Communication | Open Access

Energy Materials

Wang *et al. Energy Mater.* **2026**, *6*, 600116 **DOI:**10.20517/energymater.2026.215

Superhydrophobicity-enabled triphase interfacial microenvironment for high-temperature CO_2-to-formate electrocatalysis

Weiyan Wang[1,#], Kaixin Li[1,#], Siyu Zou[2,#], Lihui Huang[1], Xia Sheng[1], Jun Zhang[1,*], Xinjian Feng[1,*]

Keywords:
CO_2 electroreduction, formate production, thermal intensification, triphase interface, mathematical modeling

Citation: Wang, W.; Li, K.; Zou, S.; Huang, L.; Sheng, X.; Zhang, J.; Feng, X. Superhydrophobicity-enabled triphase interfacial microenvironment for high-temperature CO_2-to-formate electrocatalysis. *Energy Mater.* **2026**, *6*, 600116. https://dx.doi.org/10.20517/energymater.2026.215

Received: 8 Jul 2026
First Decision: 22 Jul 2026
Revised: 12 Aug 2026
Accepted: 20 Aug 2026
Published: 15 Sep 2026

Academic Editor:
Yuping Wu
Copy Editor:
Ping Zhang
Production Editor:
Ping Zhang

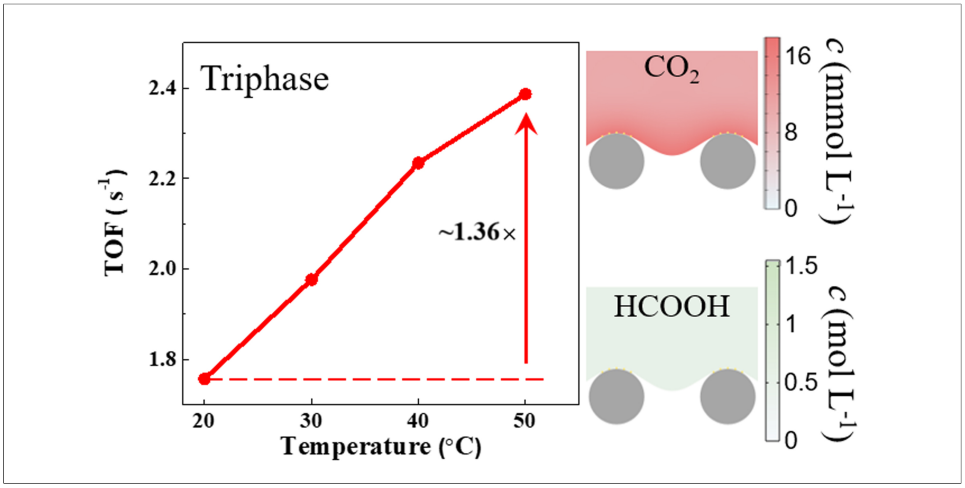

Abstract

Thermal intensification of CO_2 electroreduction to the key feedstock formate is thermodynamically favorable; however, its practical utility is often compromised by solubility-driven CO_2 depletion and parasitic hydrogen evolution. Here, we develop a solid-liquid-gas triphase boundary (TPB) to circumvent this limitation. This architecture decouples the CO_2 supply from bulk solubility constraints, ensuring reactant availability under thermal activation. Electrochemical evaluation demonstrates that the TPB electrode maintains a Faradaic efficiency exceeding 80% at high temperature, along with a significant increase in formate production rate. Kinetic analyses reveal a distinct mechanistic divergence, showing that the TPB enhances turnover frequency (TOF) by 36% at 50 °C relative to 20 °C, whereas the conventional biphasic system suffers a 70% TOF decline. Mechanistic simulations indicate that the TPB sustains near-saturated interfacial CO_2 concentrations while facilitating rapid formate expulsion at elevated temperatures, thereby preventing product accumulation. This work presents a viable strategy for

[1]State Key Laboratory of Bioinspired Interfacial Materials Science, College of Chemistry, Chemical Engineering and Materials Science, Soochow University, Suzhou 215123, Jiangsu, China.
[2]College of Chemical Engineering, Xiangtan University, Xiangtan 411105, Hunan, China.
[#]These authors contributed equally to this work.

[*]**Correspondence to:** Prof. Xinjian Feng, Dr. Jun Zhang, State Key Laboratory of Bioinspired Interfacial Materials Science, College of Chemistry, Chemical Engineering and Materials Science, Soochow University, Suzhou 215123, Jiangsu, China. E-mail: xjfeng@suda.edu.cn; jzhang2017@suda.edu.cn

thermally intensified electrocatalysis by integrating material superhydrophobicity with thermal kinetics.

INTRODUCTION

Electrocatalytic CO_2 reduction (eCO_2RR) represents a promising strategy for converting waste CO_2 into useful chemicals, while advancing carbon neutrality and sustainable energy cycles[1-4]. Unlike many multi-carbon hydrocarbon products from eCO_2RR that exhibit low faradaic efficiencies, formate represents one of the most commercially viable targets[5], owing to its broad utility in industrial synthesis and energy-related applications. Despite significant advances in catalyst design, the practical application of this technology remains constrained not only by sluggish reaction kinetics[6-10], but also by detrimental formate accumulation at active sites, which degrades the interfacial microenvironment and promotes the hydrogen evolution reaction (HER)[11-13]. Unfortunately, conventional optimization strategies centered on catalyst or electrolyte modification offer limited leverage over the inherent reaction-diffusion constraints[14-17] and are often insufficient to simultaneously enhance the intrinsic catalytic turnover and mitigate the mass transport bottleneck imposed by formate accumulation.

Recent advances highlight thermal activation as an attractive strategy for enhancing catalytic activity and alleviating product accumulation[18,19], thereby addressing the dual challenges of conventional eCO_2RR systems. Nevertheless, the thermodynamic benefit of heating is compromised by the concomitant reduction in CO_2 solubility, leading to severe mass transport limitations due to reactant depletion at the electrode interface[20,21]. This transport bottleneck is further aggravated by the Arrhenius-type acceleration of the competing HER, which excessively consumes protons and electrons[22-24]. Although this thermally driven desorption is beneficial for formate removal, it occurs alongside the solubility-driven CO_2 deficit and HER acceleration mentioned above, creating a complex trade-off that thus constrains its performance[25-28]. Consequently, this inherent conflict imposes both thermodynamic and kinetic constraints, effectively limiting high-performance electrocatalysis to a narrow near-ambient temperature window[29-31].

As an interface-dominated process, eCO_2RR suffers from severe mass transport limitations arising from the low solubility and slow diffusion of CO_2 in aqueous electrolytes. To address this, constructing solid-liquid-gas triphase boundaries (TPBs) has emerged as an effective strategy for achieving localized CO_2 enrichment at the catalyst surface, thereby significantly enhancing the CO_2 supply capability at the catalyst/electrolyte interface[32-35]. By stabilizing a persistent gas film atop superhydrophobic scaffolds, TPBs decouple the interfacial reactant supply from bulk solubility constraints and concurrently modulate the local hydration environment to mitigate parasitic reactions. While previous TPB-based studies have predominantly focused on mitigating reactant (CO_2) starvation at ambient temperatures, the impact of thermal activation on product expulsion dynamics remains largely unexplored. When applied to thermally activated systems, this architecture uniquely enables management of the complex interplay between thermal kinetics and mass transport[36,37]. The inherent hydrophobic confinement preserves gaseous reactant (CO_2) channels at elevated temperatures, allowing the thermally enhanced diffusion kinetics to be specifically leveraged for accelerating product expulsion from the interface[38,39].

Inspired by these advances, herein we propose a catalyst-integrated, superhydrophobic TPB architecture that resolves the conflict inherent in thermal activation for high-efficiency CO_2-to-formate conversion. As illustrated in Figure 1, the superhydrophobic substrate establishes a gas/liquid dual-transport pathway. This design utilizes the gas channel (red arrow) to compensate for the solubility-driven CO_2 depletion in the liquid phase (blue arrow) and leverages elevated temperatures to accelerate formate desorption (black arrow), thereby ensuring optimal utilization of thermal intensification strategies. Electrochemical evaluation

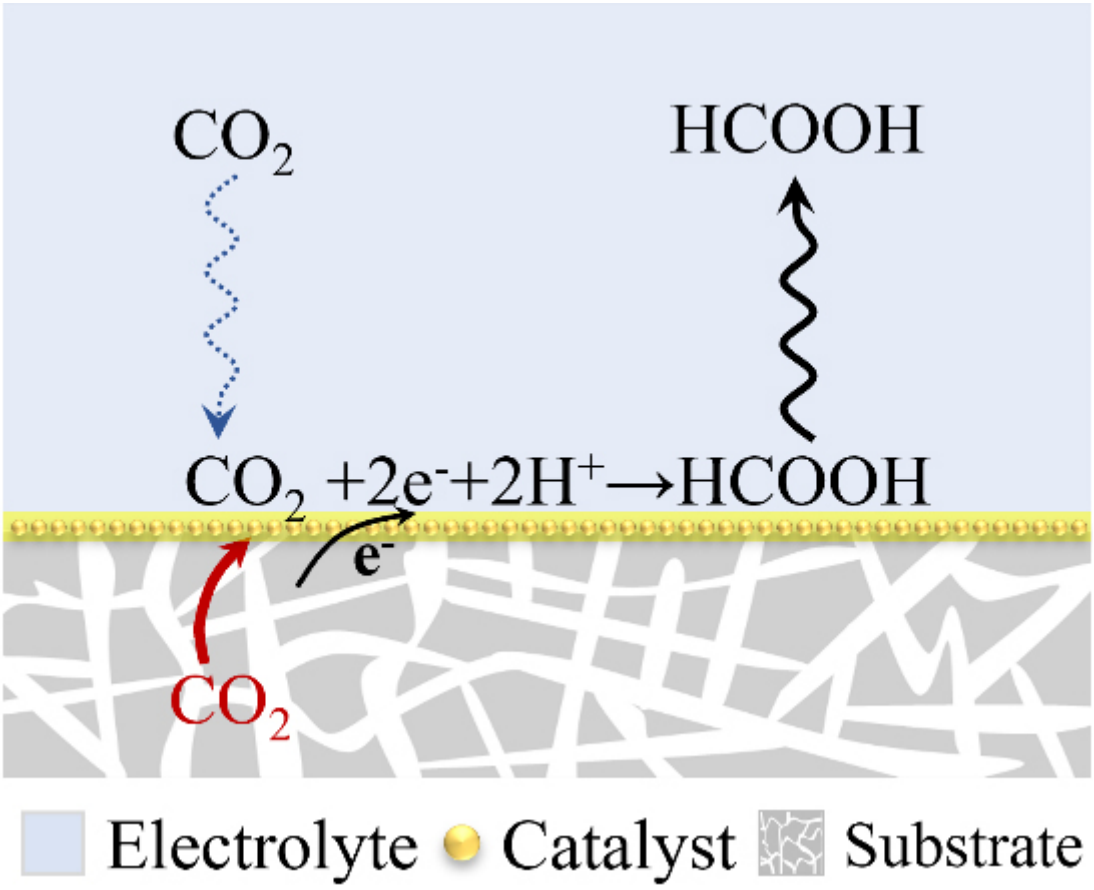

Figure 1. Schematic illustration of the solid-liquid-gas triphase interface for thermally intensified CO_2 electroreduction to formate. With the gas channel (red arrow) providing a sufficient supply to counteract the solubility-driven CO_2 depletion in the liquid phase (blue arrow), the elevated temperature accelerates formate desorption (black arrow), synergistically ensuring the maximal utilization of thermal intensification strategies.

reveals that, in stark contrast to conventional diphase systems where HER dominates upon heating, our TPB electrode achieves a 1.7-fold increase in formate production rate at 50 °C relative to 20 °C, while maintaining a Faradaic efficiency above 80%. Steady-state multiphysics simulations were employed to quantify the interfacial CO_2 and formate distributions within different microenvironments under thermal activation. This work addresses this gap by elucidating how elevated temperatures actively leverage the triphase boundary to accelerate product desorption, thereby presenting a dual-regulation strategy for thermally intensified CO_2 electroreduction. The results confirm that the gas channel sustains near-saturated CO_2 concentrations precisely at the reaction interface, effectively offsetting the thermally induced solubility loss in the bulk liquid. This dual-regulation mechanism simultaneously addresses both the CO_2 supply deficiency and the adverse effect of product accumulation. By maintaining robust CO_2 delivery and rapid product removal, this design overcomes the inherent mass-transport bottlenecks of thermal intensification, ensuring high-efficiency formate production.

EXPERIMENTAL

Chemicals

Polytetrafluoroethylene (PTFE) treated carbon substrate (AvCarb GDS1120) was bought from Fuel Cell Store. Indium acetylacetonate (99.99%), anhydrous ethanol and Potassium bicarbonate ($KHCO_3$) were bought from Sigma-Aldrich. CO_2 and N_2 gases with high purity (99.99%) were used for the electrocatalytic measurements. All chemicals were directly used without further purification. All solutions were prepared

with Milli-Q water (18.2 MΩ).

Electrode preparation

Porous superhydrophobic carbon paper was used as the substrate. Indium acetylacetonate (3.6 mg) was dissolved in 200 μL of anhydrous ethanol and ultrasonicated to obtain a homogeneous solution. The indium precursor solution was drop-cast onto the central 2 × 2 cm^2 area of a 3 × 3 cm^2 hydrophobic carbon paper placed on a 90 °C heating plate. The electrode was then dried in an oven at 80 °C for 1 h, followed by calcination in a muffle furnace at 300 °C for 1 h. After cooling to room temperature, it was electrochemically reduced in situ under potentiostatic conditions to obtain triphase electrodes decorated with In nanoparticles (In-3P). Finally, the surface of the triphase electrode was treated by oxygen plasma sputtering to render it hydrophilic, yielding a diphase electrode (In-2P).

Characterization instrumentation

Electrochemical measurements were carried out using a CHI-660E electrochemical workstation (Shanghai Chenhua Instruments Co., Ltd., China). Gas chromatography (GC) analysis was performed on an Agilent 7890B gas chromatograph. Nuclear Magnetic Resonance (NMR) spectra were recorded on a Bruker AVANCE III NMR spectrometer (Bruker, Germany). Scanning Electron Microscope (SEM) characterization was conducted using a Hitachi S-4800 scanning electron microscope (Hitachi, Japan). Transmission Electron Microscope (TEM) characterization was performed on an Field Electron and Ion Company (FEI) Tecnai G2 F20 transmission electron microscope (FEI, USA). X-ray diffraction (XRD) measurements were performed on a SmartLab 3 kW multi-purpose X-ray diffractometer (Rigaku, Japan).

RESULTS AND DISCUSSION

To realize the triphase interface concept depicted in Figure 1, we engineered an integrated electrode architecture wherein the catalyst is embedded within a stabilized triphase microenvironment [Figure 2A]. The fabrication commenced with a commercial hydrophobic carbon fiber paper pre-loaded with hydrophobic carbon particles, which served as a conductive backbone and imparted the necessary surface roughness to ensure superhydrophobicity. This hierarchical roughness enables the substrate to trap a stable gas film, thereby establishing the triphase interface essential for the efficient catalysis. Field emission scanning electron microscope (FE-SEM) imaging [Figure 2B] reveals the hierarchical micro/nano-structure, while the accompanying water contact angle measurement of 146 ± 2° (Figure 2B, inset) confirms the surface's exceptional hydrophobicity, guaranteeing the formation of a stable gas film upon immersion[40,41].

Indium (In) nanoparticles, serving as a model electrocatalyst for CO_2 conversion into formate, were loaded onto the superhydrophobic carbon substrate via a thermal decomposition procedure, followed by in situ electrochemical reduction to yield the triphase electrode. Following the immobilization of In nanoparticles, the electrode surface exhibited a water contact angle (CA) of 142 ± 2° [Supplementary Figure 1], confirming its robust hydrophobic nature. As shown in Figures 2C and Supplementary Figure 2, these In nanoparticles (10~30 nm) are uniformly dispersed across the carbon particle surfaces. This uniform distribution is further substantiated by energy-dispersive X-ray spectroscopy (EDS) elemental mapping [Figure 2D], which verifies the homogeneous spatial distribution of In signals across the electrode area, corroborating consistent catalyst loading. XRD pattern in Figure 2E exhibits distinct peaks that correspond precisely to the standard reference pattern for body-centered tetragonal metallic indium (PDF#85-1409), confirming the successful synthesis and crystallinity of the In catalyst. These characterizations confirm the successful fabrication of the targeted triphase electrode architecture, which maintains a stable solid-liquid-gas microenvironment during electrolysis and serves as a robust platform for high-temperature CO_2 electroreduction studies. For comparison, a diphase electrode (In-2P) was prepared by subjecting the triphase In electrode (In-3P) to O_2 plasma treatment. As shown in Supplementary Figure 3, this treated surface became hydrophilic, exhibiting a

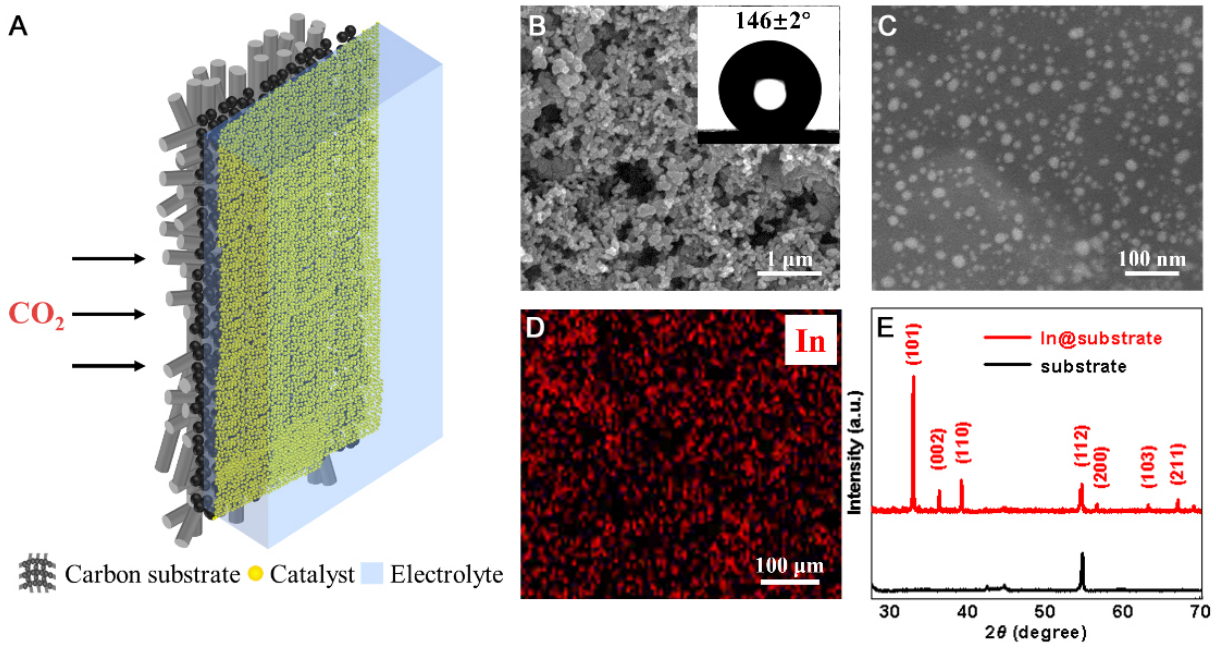

Figure 2. (A) Schematic illustration of the catalyst-integrated, superhydrophobic carbon-based TPB architecture; (B) Field emission scanning electron microscope (FE-SEM) of the superhydrophobic carbon substrate. The inset shows a water droplet placed on the substrate with a water contact angle of approximately 146 ± 2°; (C) FE-SEM of the In nanoparticles immobilized on the carbon substrate; (D) EDS elemental maps of In element; (E) XRD patterns of carbon substrate and In@substrate. EDS: Energy-dispersive X-ray spectroscopy; TPB: triphase boundary; XRD: X-ray diffraction; SEM: scanning electron microscope.

water contact angle of 21 ± 2°.

Following structural characterizations of the as-prepared electrode, we evaluated its thermally activated electrocatalytic activity via potential-resolved chronoamperometric tests [Supplementary Figures 4 and 5]. The electrocatalytic CO_2 reduction performance was evaluated at different temperatures in CO_2-saturated 0.5 M $KHCO_3$. Prior to each test, the entire assembly - including the electrode, electrolyte, and cell - was preheated to the target temperature in a water bath under a continuous CO_2 flow. Steady-state current densities were extracted from the acquired i-t profiles at different applied potentials [Figure 3]. Figure 3A illustrates that the In-3P electrode yields steady, monotonically increasing current densities as temperature rises throughout the measured potential range. At -0.8 V *vs.* Reversible Hydrogen Electrode (RHE) as a representative point, current density rises substantially from -15 mA cm^{-2} at 20 °C up to -26 mA cm^{-2} at 50 °C. This observation confirms that the triphase boundary suppresses local CO_2 starvation, enabling thermal energy to continuously boost catalytic currents without encountering mass-transport-limited saturation[42]. By comparison, the conventional diphase In-2P electrode exhibits markedly diminished performance enhancements upon heating [Figure 3B]. Notably, improvements remain negligible at potentials anodic of -0.8 V *vs.* RHE; within this potential window, raising the temperature from 20 °C to 50 °C elicits little to no increase in measured current densities. Such behavior demonstrates that mass-transport constraints impose an insurmountable upper limit on activity, as the decline in CO_2 solubility at higher temperatures negates kinetic advantages from thermal activation.

To decouple contributions to the measured current between target CO_2 reduction and parasitic hydrogen evolution (HER), product speciation was quantified via in-line gas chromatography and post-reaction NMR characterization [Supplementary Figures 6 and 7]. Over the full range of measured temperatures and potentials, the In-3P catalyst sustains remarkably high formate selectivity, with Faradaic efficiencies for formate (FE-HCOOH) consistently above 80% [Figure 3C]. Quantitatively, the formate partial current

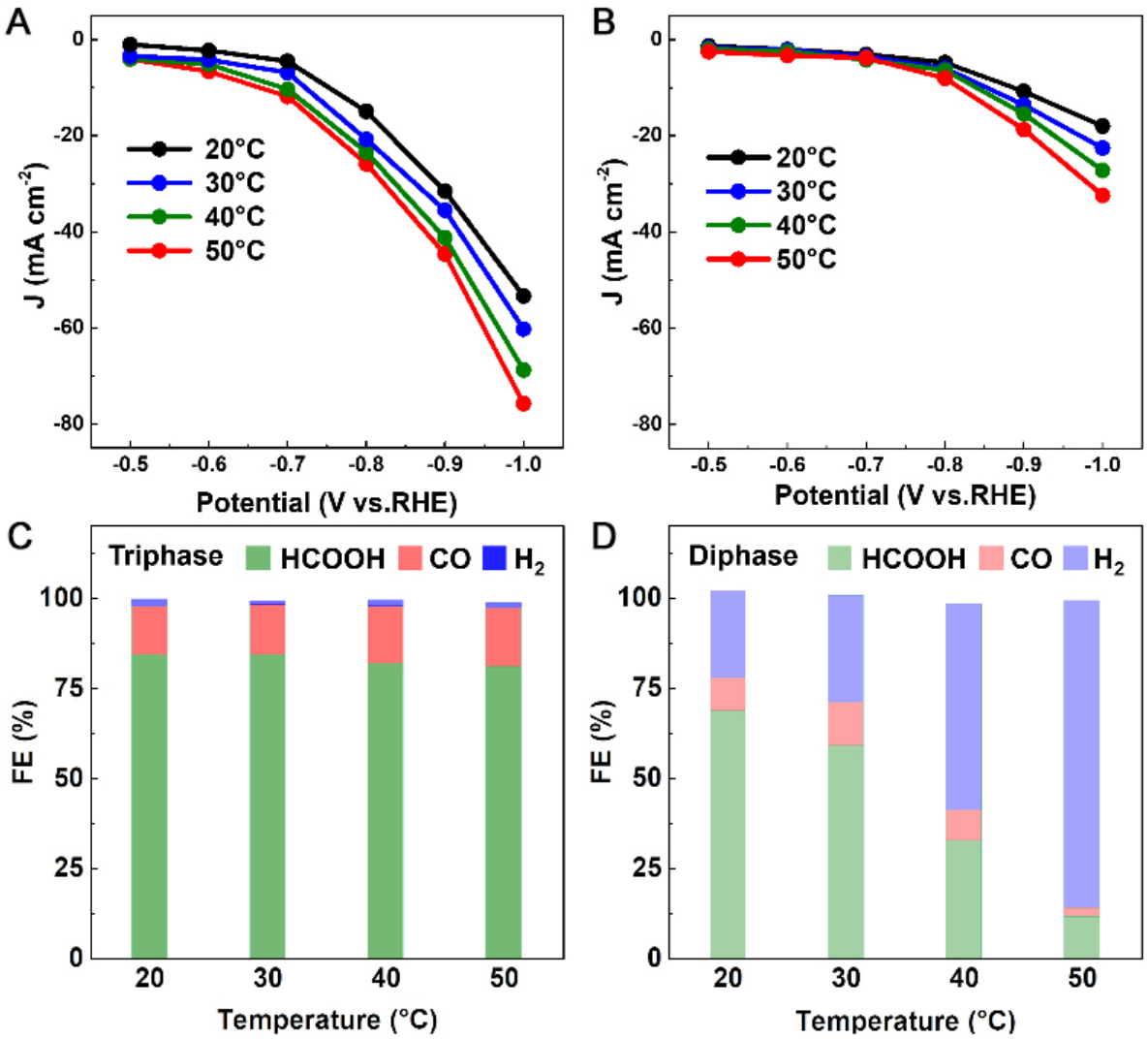

Figure 3. (A and B) Total current densities for the CO_2RR achieved using the triphase and diphase electrodes, respectively, at various potentials and temperatures; (C) FE of CO_2RR products on In-3P electrode at a potential of -0.9 V *vs.* RHE and various temperatures; (D) FE of CO_2RR products on In-2P electrode at a potential of -0.9 V *vs.* RHE and various temperatures. CO_2RR: CO_2 reduction reaction; FE: Faradaic efficiency; RHE: reversible hydrogen electrode.

density (J-HCOOH) increases by a factor of ~1.7 as the temperature rises from 20 °C to 50 °C, corresponding to an ~1.7-fold increase in formate production [Supplementary Figure 8], a performance enhancement ranking among the competitive results for high-temperature CO_2-to-formate conversion[43-46]. This firmly validates that the thermally amplified currents plotted in Figure 3A originate from faster CO_2-to-formate conversion rather than HER. Though heating increases local proton availability and typically favors HER, the triphase boundary modulates the near-electrode microenvironment to effectively suppress competing hydrogen evolution. Conversely, the In-2P electrode suffered a precipitous loss in selectivity upon heating [Figure 3D]. While a reasonable FE-HCOOH (~70%) was sustained at 20 °C, it declined with increasing temperature. At 50 °C and -0.9 V *vs.* RHE, hydrogen evolution nearly dominates the entire electrolysis process, yielding FE-HCOOH below 12%. Such results confirm that the thermal current gain in typical diphase systems primarily originates from parasitic HER activity. To further decouple the role of the gaseous CO_2 pathway from potential substrate modifications introduced during electrode fabrication, we conducted a control experiment using the pristine In-3P electrode (In-3P-N_2). In this configuration, the gas chamber was purged with inert N_2 while CO_2 was supplied exclusively through the liquid electrolyte. This approach

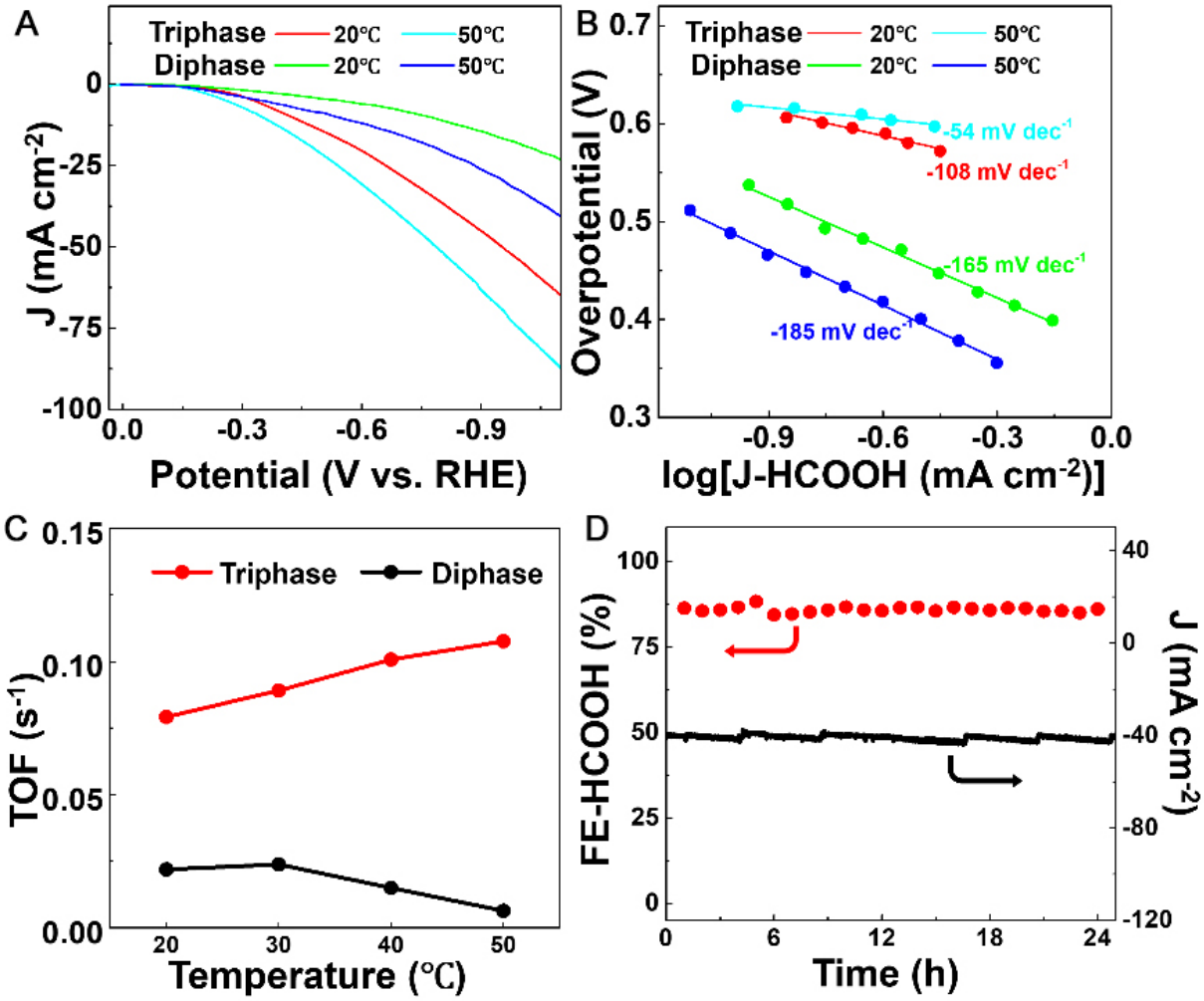

Figure 4. (A) LSV curves for triphase and diphase electrodes at 20 °C and 50 °C; (B) Tafel analyses of the partial current densities for formate production; (C) Apparent turnover frequency (TOF) of HCOOH production at -0.9 V *vs.* RHE under various temperatures; (D) Stability of In-3P electrode at -0.9 V *vs.* RHE and 40 °C. LSV: Linear sweep voltammetry; FE: Faradaic efficiency; RHE: reversible hydrogen electrode.

preserves the native surface chemistry of the catalyst and carbon scaffold while solely removing the gas-phase reactant supply. As demonstrated in Supplementary Figures 9 and 10, the In-3P-N_2 electrode mirrors the In-2P performance trajectory, exhibiting increased current density with temperature but a sharp decline in formate selectivity as HER dominates at elevated temperatures. This convergence confirms that the absence of a gaseous CO_2 pathway is the determining factor governing high-temperature selectivity.

The markedly different temperature-dependent behaviors in the diphase and triphase systems using the same catalyst can be attributed to their distinct interfacial microenvironments, which modulate the local availability of CO_2 and H_2O at the reaction interface. To explore this difference further, the electrochemical responses of both electrodes were examined at various temperatures. As shown in Figure 4A, the linear sweep voltammetry (LSV) profiles were recorded in CO_2-saturated electrolyte at varying temperatures. In line with the trends shown in Figure 3, heating boosts current densities for both electrodes, demonstrating that thermal promotion of reaction kinetics applies to both systems. Notably, the In-3P electrode delivers substantially higher catalytic currents than the In-2P counterpart under identical thermal conditions, highlighting the mass-transport advantages of the triphase design.

To further understand the distinct activity and selectivity at elevated temperatures, Tafel analysis was performed on the formate partial current densities of both electrodes at 20 °C and 50 °C [Figure 4B], derived from the LSV profiles [Figure 4A] and corresponding Faradaic efficiencies. The In-3P electrode exhibited a marked shift toward less negative Tafel slopes, from -108 to -54 mV dec^{-1}, as the temperature increased from 20 °C to 50 °C. This shift confirms that the triphase design mitigates the reactant depletion typically exacerbated at high temperatures, effectively accelerating the intrinsic kinetics of formate formation. This behavior is attributed to the ability of the triphase boundary to sustain near-saturated interfacial CO_2 while simultaneously alleviating local product accumulation. By decoupling the reaction zone from bulk mass-transport constraints, thermal energy is channeled into accelerating the intrinsic catalytic turnover rather than being dissipated by kinetic bottlenecks. In contrast, the In-2P electrode exhibited a marked shift toward more negative Tafel slopes, from -165 mV dec^{-1} at 20 °C to -185 mV dec^{-1} at 50 °C. This change indicates that the kinetic acceleration from thermal activation is largely negated by intensified mass-transport limitations and parasitic HER. The increasing slope magnitude quantitatively reflects the intensified competition between HER and CO_2 reduction, highlighting the system's inability to utilize thermal energy for the target reaction without a gaseous CO_2 supply. These results demonstrate that the rationally designed triphase interface successfully transforms thermal energy from a performance-limiting factor in conventional aqueous electrocatalysis into a powerful amplifier for boosting target CO_2 reduction kinetics.

The intrinsic advantage of the triphase architecture emerges clearly when examining the turnover frequency (TOF) for formate production shown in Figure 4C. Notably, the TOF values reported herein represent apparent TOF, calculated based on the total moles of In precursor loaded during fabrication and assuming quantitative conversion to metallic In. While the In-3P electrode exhibits a monotonic TOF increase from 0.079 s^{-1} at 20 °C to 0.108 s^{-1} at 50 °C, the In-2P electrode follows an opposite trend, with its TOF decreasing from 0.022 s^{-1} to 0.0064 s^{-1}. This difference reveals a fundamental mechanistic shift that aligns with the observations in the selectivity data in Figure 3. Conversely, the diphase electrode undergoes a thermally driven decay in apparent intrinsic activity, countering the acceleration in reaction kinetics and resulting in only marginal current increase. More critically, the loss of intrinsic activity correlates with the significant deterioration in selectivity, where thermally enhanced HER outcompetes CO_2 reduction under reactant-starved conditions. Therefore, the triphase design overcomes the typical activity-selectivity trade-off in high-temperature CO_2 electroreduction by directing thermal energy specifically into the target reaction pathway. Chronoamperometry at -0.9 V *vs.* RHE and 40 °C shows a steady current density over 24 h, with the Faradaic efficiency for formate remaining above 80% [Figure 4D]. Post-test characterization [Supplementary Figure 11] confirms the intact chemical state and structural robustness of the catalyst, with only a marginal decline in surface hydrophobicity after the 24 h test. This operational durability highlights the thermostability of the triphase design for continuous, high-efficiency CO_2 electroreduction. While these results are highly encouraging for industrial translation, future long-term operation warrants monitoring for potential hydrophobic scaffold evolution and possible trace In leaching under extended cathodic biases.

To further understand the effect of interfacial architecture on reactant and product distributions, a continuum-scale multiphysics model was constructed to simulate the steady-state concentration profiles within the diphase and triphase systems [Figure 5A, Supplementary Figure 12 and Supplementary Table 1]. It is important to note that this simulation framework was constructed to deconvolute experimental observations rather than to predict unknown phenomena. The computational domain for the triphase system comprises a gas diffusion layer (GDL), a catalyst layer (CL), a liquid diffusion layer (LDL), and the underlying substrate. The model incorporates species diffusion (including CO_2), CO_2 dissolution, and formate production. Species transport is described by Fick's law. CO_2 dissolution from the gas phase to the liquid phase is described by Henry's law [Supplementary Table 2]. The catalytic reaction for formate production is modeled as first-order kinetics with respect to the interfacial formate concentration. This

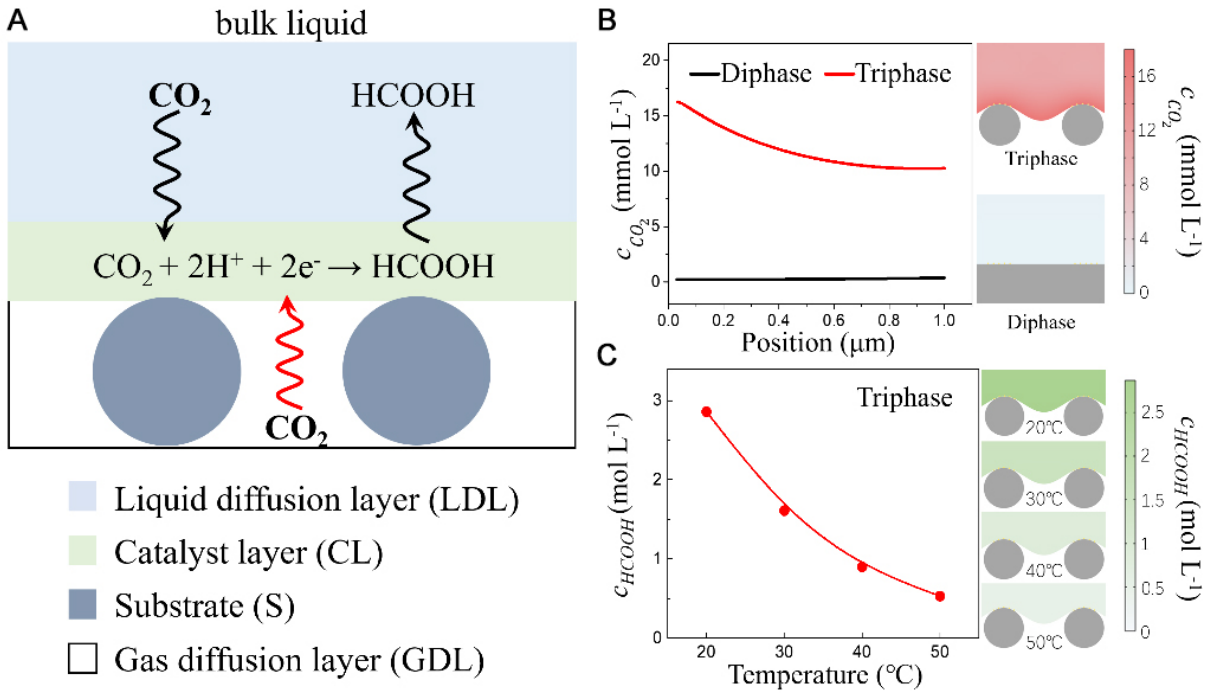

Figure 5. (A) The schematic diagram of the computational domain with boundary indicators; (B) Simulated CO_2 concentration profiles as a function of distance from the triphase interface into the solution for the triphase (red) and diphase (black) systems at 50 °C. Diagram on the right is CO_2 concentration diffusion model in the triphase (the upper) and diphase (the lower) systems; (C) Simulated local formate concentration at the reaction interface as a function of temperature in the triphase system. Diagram on the right is the formate concentration diffusion model.

formulation is dictated by the pronounced shift toward less negative Tafel slopes at elevated temperatures, which signifies a transition to a rate-determining step no longer limited by the accumulation of reaction products. This rate law ensures the model captures the decoupling of kinetics from bulk solubility constraints under thermal activation.

Figure 5B shows the simulated results of CO_2 concentration (c_{CO_2}) distribution in the catalytic zone during the reaction for diphase and triphase systems at 50 °C, where the abscissa denotes the distance from the substrate/liquid interface. For the diphase system, the CO_2 concentration is critically low at the interface (~0.22 mmol L^{-1}) and gradually increases with distance into the electrolyte, reaching ~0.37 mmol L^{-1}. This profile arises from the combined effects of reduced CO_2 solubility at 50 °C and continuous reactant consumption at the electrode interface. The diminished bulk concentration establishes a low baseline, while interfacial consumption generates a concentration gradient. Consequently, regions distal to the interface retain relatively higher CO_2 levels due to the attenuated depletion away from the catalytic surface. The entire reaction zone therefore remains in a CO_2-deficient state. In contrast, for the triphase system with direct gas-phase CO_2 supply, the concentration decreases with distance but remains substantially higher than that in the diphase system. CO_2 at the solid-liquid-gas interface (x = 0) approaches saturation (~17.21 mmol L^{-1}). Therefore, even under the elevated reaction rates induced by high temperature (50 °C), the CO_2 concentration remains above 10 mmol L^{-1} throughout the entire reaction zone, sustaining a robust supply consistent with the high catalytic activity measured in the TOF tests.

Furthermore, we investigated the local formate concentration (c_{HCOOH}) within the triphase microenvironment as a function of temperature [Figure 5C]. While the formate production rate increases with temperature, the simulated formate concentration at the interface decreases systematically from 20 °C to 50 °C. This counterintuitive trend arises because the thermally enhanced diffusion coefficient exceeds the increased

formate generation rate, thereby facilitating rapid product evacuation from the interface. This reduction in interfacial accumulation mitigates the inhibitory effect of formate accumulation on the active sites, thereby sustaining the high intrinsic activity of CO_2 reduction. Figure 5C shows the simulated interfacial formate concentration drops sharply from 2.86 mol L^{-1} at 20 °C to 0.53 mol L^{-1} at 50 °C. This severe depletion at the catalytic interface implies that product removal is no longer the bottleneck; rather, the reaction rate is now dictated by the intrinsic surface kinetics.

Crucially, this simulation prediction is experimentally validated by the flow-rate analysis shown in Supplementary Figure 13. The current response exhibited a distinct evolution with temperature. At 20~30 °C, the steady-state current decreased with increasing flow rate, attributed to shear-induced compression of hydrophobic gas cavities that reduces the effective triple-phase boundary area. At 40 °C, the trend reversed, with current increasing until reaching a plateau above 15 mL min^{-1}. Most significantly, at 50 °C, the current plateaued at an even lower flow rate of 10 mL min^{-1}. This progression indicates that mass-transport limitations are progressively alleviated at elevated temperatures. The observation that the current becomes insensitive to flow rates above 10 mL min^{-1} at 50 °C aligns with simulations showing a marked depression of interfacial formate concentration. This experimental plateau serves as empirical evidence that thermally accelerated diffusion effectively evacuates interfacial products, thereby decoupling the reaction kinetics from convective supply and underpinning the high efficiency for formate production. Consequently, these results confirm that the triphase architecture maintains a favorable microenvironment at elevated temperatures, characterized by both high reactant supply and low product retention, which underpins the high efficiency for formate production.

CONCLUSIONS

In this work, we constructed a solid-liquid-gas triphase boundary (TPB) architecture to address the inherent conflict between kinetic acceleration and mass-transport limitations in thermally intensified CO_2 electroreduction to formate. A catalyst-integrated, superhydrophobic carbon scaffold was fabricated and deployed as the TPB electrode. The triphase design established a unique solid-liquid-gas microenvironment that decoupled the interfacial CO_2 supply from bulk solubility constraints. Multiphysics simulations demonstrate that the TPB sustains near-saturated CO_2 concentrations at the reaction interface, effectively counteracting the solubility-driven reactant depletion observed in conventional diphase systems, thereby achieving a ~1.36-fold enhancement in apparent TOF at 50 °C relative to 20 °C. Moreover, the triphase system harnesses thermal energy to accelerate formate expulsion, mitigating product accumulation and further boosting the overall reaction efficiency. These results highlight the critical role of interfacial microstructure engineering in reconciling mass-transport constraints with thermal kinetic enhancement for selective CO_2 electroreduction.

DECLARATIONS

Authors' contributions

Conceptualization, methodology, investigation, data curation, formal analysis: Wang, W.; Li, K.; Zou, S.; Huang, L.; Sheng, X.

Conceptualization, methodology, investigation, formal analysis, funding acquisition, supervision: Zhang, J.; Feng, X.

Availability of data and materials

The data supporting the findings of this study are available within this Article and its Supplementary Materials. Further data are available from the corresponding authors upon request.

AI and AI-assisted tools statement

Not applicable.

Financial support and sponsorship

This research was financially supported by the National Natural Science Foundation of China (22572139 and 22102111), the National Key Research and Development Program of China (2019YFA0709200), and Suzhou Key Laboratory of Spent Lithium Battery Recycling (SZS2025005).

Conflicts of interest

All authors declared that there are no conflicts of interest.

Ethical approval and consent to participate

Not applicable.

Consent for publication

Not applicable.

Copyright

Supplementary Materials

Supplementary Materials

REFERENCES

1. Li, J.; Wang, H.; Zhang, C.; et al. A high-flux membrane electrode assembly for CO_2 electroreduction to 4.5 M formate with over 8,000 h stability. *Nat. Catal.* **2026**, *9*, 492-501. DOI
2. Belsa, B.; Xia, L.; Golovanova, V.; et al. Materials challenges on the path to gigatonne CO_2 electrolysis. *Nat. Rev. Mater.* **2024**, *9*, 535-49. DOI
3. Ma, T.; Jiao, Z.; Qiu, H.; Wang, F.; Liu, Y.; Guo, L. Synergistic effect of oxygen species and vacancy for enhanced electrochemical CO_2 conversion to formate on indium oxide. *eScience* **2024**, *4*, 100246. DOI
4. Zhang, M.; Cao, A.; Xiang, Y.; et al. Strongly coupled Ag/Sn-SnO_2 nanosheets toward CO_2 electroreduction to pure HCOOH solutions at ampere-level current. *NanoMicro. Lett.* **2023**, *16*, 50. DOI
5. Sun, S.; Mao, Y.; Liu, F.; et al. Recent advances in nanoscale engineering of Pd-based electrocatalysts for selective CO_2 electroreduction to formic acid/formate. *Energy. Mater.* **2024**, *4*, 400027. DOI
6. Liu, J.; Duan, R.; Xu, Y.; et al. Decoupled control of CO_2 and nitrate reduction intermediates to enable efficient tandem urea electrosynthesis. *ACS. Nano.* **2025**, *19*, 29646-56. DOI
7. Kim, J. Y. T.; Zhu, P.; Chen, F.; Wu, Z.; Cullen, D. A.; Wang, H. Recovering carbon losses in CO_2 electrolysis using a solid electrolyte reactor. *Nat. Catal.* **2022**, *5*, 288-99. DOI
8. Qiu, C.; Qian, K.; Yu, J.; et al. MOF-transformed In_2O_{3-x}@C nanocorn electrocatalyst for efficient CO_2 reduction to HCOOH. *NanoMicro. Lett.* **2022**, *14*, 167. DOI PubMed PMC
9. Xu, H.; Wang, J.; He, H.; et al. Modulating CO_2 electrocatalytic conversion to the organics pathway by the catalytic site dimension. *J. Am. Chem. Soc.* **2024**, *146*, 10357-66. DOI
10. Tan, J.; Shelton, J. L.; Wright, D.; et al. Chirality-induced spin selectivity as a mechanism to control product selectivity during electrochemical CO_2 reduction. *Nat. Energy.* **2026**, *11*, 1151-60. DOI
11. Abarca, J. A.; Warmuth, L.; Rieder, A.; et al. GDE stability in CO_2 electroreduction to formate: the role of ionomer type and loading. *ACS. Catal.* **2025**, *15*, 8753-67. DOI
12. Singh, C.; Song, J.; Prasannachandran, R.; et al. Unlocking long-term stability in metal-based gas diffusion electrodes for CO_2 electroreduction. *EES. Catal.* **2026**, *4*, 97-107. DOI
13. Yang, H.; Cai, H.; Song, K.; et al. Constructing monolayer fe clusters as model catalysts for CO_2 electroreduction. *J. Am. Chem. Soc.* **2025**, *147*, 32494-501. DOI
14. Sullivan, I.; Goryachev, A.; Digdaya, I. A.; et al. Coupling electrochemical CO_2 conversion with CO_2 capture. *Nat. Catal.* **2021**, *4*, 952-8. DOI
15. Dutta, N.; Peter, S. C. Electrochemical CO_2 reduction in acidic media: a perspective. *J. Am. Chem. Soc.* **2025**, *147*, 9019-36. DOI
16. Dong, J.; Chen, J.; Wang, W.; Wei, Z.; Tian, Z. Q.; Fan, F. R. Charged microdroplets as microelectrochemical cells for CO_2 reduction and C-C coupling. *J. Am. Chem. Soc.* **2024**, *146*, 2227-36. DOI

17. Zhong, S.; Cao, Z.; Yang, X.; et al. Electrochemical conversion of CO_2 to 2-bromoethanol in a membraneless cell. *ACS. Energy. Lett.* **2019**, *4*, 600-5. DOI
18. Bian, X.; Zhao, Y.; Waterhouse, G. I. N.; et al. Quantifying the contribution of hot electrons in photothermal catalysis: a case study of ammonia synthesis over carbon-supported ru catalyst. *Angew. Chem. Int. Ed.* **2023**, *62*, e202304452. DOI
19. Wang, J.; Yuan, X.; Devasenathipathy, R.; et al. Unveiling plasmonic heating effect on the electrochemical response of gold nanostructured electrode via experiment and multiphysics simulation. *Electrochim. Acta.* **2023**, *464*, 142899. DOI
20. Xiong, J.; Ji, J.; Lei, Q.; et al. Synergetic energy coupled thermal catalytic systems for CO_2 reduction. *eScience* **2025**, *5*, 100306. DOI
21. Pelzer, H. M.; Kolobov, N.; Vermaas, D. A.; Burdyny, T. Scaling and heating will drive low-temperature CO_2 electrolysers to operate at higher temperatures. *Nat. Energy.* **2025**, *10*, 549-56. DOI
22. Bienen, F.; Kopljar, D.; Geiger, S.; Wagner, N.; Friedrich, K. A. Investigation of CO_2 electrolysis on tin foil by electrochemical impedance spectroscopy. *ACS. Sustainable. Chem. Eng.* **2020**, *8*, 5192-9. DOI
23. Vos, R. E.; Sun, P.; Schauermann, D.; et al. CO_2 electroreduction on Cu operates via an alternative chain growth mechanism to form C-C bonds at elevated temperature and pressure. *Nat. Catal.* **2025**, *8*, 1338-47. DOI
24. Díaz-sainz, G.; Alvarez-guerra, M.; Irabien, A. Continuous electroreduction of CO_2 towards formate in gas-phase operation at high current densities with an anion exchange membrane. *J. CO2. Util.* **2022**, *56*, 101822. DOI
25. Hu, F.; He, B.; Chen, K.; et al. Single-atom anchored on perovskite with strong metal-oxide interaction for efficient high temperature CO_2 electrolysis. *Adv. Mater.* **2026**, *38*, e12310. DOI
26. Mohanty, A.; Viet, C. D.; Roger, A.; et al. Structural impact of carbon nanofibers/few-layer-graphene substrate decorated with Ni for CO_2 methanation via inductive heating. *Appl. Catal. B. Environ.* **2021**, *298*, 120589. DOI
27. Ye, D.; Wu, Z.; Wang, T.; et al. Anti-sintering Ni-W catalytic layer on reductive tungsten carbides for superior high-temperature CO_2 reduction. *Adv. Mater.* **2025**, *37*, e2504431. DOI
28. Zeng, M.; Zou, S.; Huang, L.; Zhang, J.; Wang, J.; Feng, X. Photothermally driven efficient CO_2 electroreduction based on a superhydrophobic electrode. *J. Am. Chem. Soc.* **2026**, *148*, 4475-83. DOI
29. Li, Y.; Shao, G.; Zheng, X.; et al. Cutting-edge advances in pressurized electrocatalytic reactors. *eScience* **2025**, *5*, 100369. DOI
30. Wang, H.; Kang, X.; Han, B. Optimizing CO_2 electroreduction: theoretical insights for enhancing efficiency across elementary steps. *Chem. Soc. Rev.* **2025**, *54*, 10156-244. DOI
31. Elgazzar, A.; Zhu, P.; Chen, F.; et al. Electrochemical CO_2 reduction to formic acid with high carbon efficiency. *ACS. Energy. Lett.* **2025**, *10*, 450-8. DOI
32. Gyenes, P.; Samu, A. A.; Hursán, D.; et al. Flooding revisited: electrolyte management ensures robust electrochemical CO_2 reduction. *Energy. Environ. Sci.* **2025**, *18*, 7124-35. DOI
33. Fan, L.; Wang, C.; Wu, Y.; et al. Synergistic electric field and confinement effects in porous Cu_2O octahedra enable CO_2 electroreduction across pH conditions. *ACS. Nano.* **2026**, *20*, 7046-57. DOI
34. Yang, P. P.; Gao, M. R. Enrichment of reactants and intermediates for electrocatalytic CO_2 reduction. *Chem. Soc. Rev.* **2023**, *52*, 4343-80. DOI PubMed
35. Dong, Y.; Xu, C.; Fu, Y.; Zhao, H.; Lei, Y. Catalyzed carbon-based materials for CO_2-battery utilization. *Energy. Mater.* **2025**, *5*, 500039. DOI
36. Löwe, A.; Rieg, C.; Hierlemann, T.; et al. Influence of temperature on the performance of gas diffusion electrodes in the CO_2 reduction reaction. *ChemElectroChem* **2019**, *6*, 4497-506. DOI
37. Sun, F.; Zhou, X.; Qin, L.; Tang, Z.; Wang, L.; Tang, Q. Probing temperature effect on enhanced electrochemical CO_2 reduction of hydrophobic $Au_{25}(SR)_{18}$ nanoclusters. *ACS. Catal.* **2025**, *15*, 4605-17. DOI
38. Jo, S.; Son, H. D.; Kim, T. Y.; et al. Ru/K_2CO_3-MgO catalytic sorbent for integrated CO_2 capture and methanation at low temperatures. *Chem. Eng. J.* **2023**, *469*, 143772. DOI
39. Sang, J.; Liu, Q.; Zhang, Y.; Liu, M. Liquid-gas interface confined AgPd nanosheets construct corn-shaped AgPd@Cu nanowires for electrochemical CO_2 reduction to C_2H_4. *Nano. Res.* **2026**, *19*, 94908282. DOI
40. Fu, H. Q.; Yu, T.; White, J.; et al. Amorphous $CuSbO_x$ composite-catalyzed electrocatalytic reduction of CO_2 to CO: CO_2 demand-supply-regulated performance. *Chem* **2025**, *11*, 102362. DOI
41. Zhang, W.; Yu, A.; Mao, H.; et al. Dynamic bubbling balanced proactive CO_2 capture and reduction on a triple-phase interface nanoporous electrocatalyst. *J. Am. Chem. Soc.* **2024**, *146*, 21335-47. DOI
42. Ma, W.; Morales-Vidal, J.; Tian, J.; et al. Encapsulated Co-Ni alloy boosts high-temperature CO_2 electroreduction. *Nature* **2025**, *641*, 1156-61. DOI

43. Pei, Y.; Gu, W.; Cheng, S.; et al. Thermo-electrochemically induced dynamic $Sn^{\delta+}$/Sn Interface for direct bicarbonate reduction to formate. *ACS. Catal.* **2023**, *13*, 12082-91. DOI

44. Rossen, A.; Daems, N.; Choukroun, D.; Breugelmans, T. Differential pressure across a gas diffusion electrode controls efficiency of liquid-fed electrolyzers for CO_2 electroreduction at elevated temperatures. *ACS. Sustainable. Chem. Eng.* **2024**, *12*, 7935-42. DOI

45. Vos, R. E.; Kolmeijer, K. E.; Jacobs, T. S.; van der Stam, W.; Weckhuysen, B. M.; Koper, M. T. M. How temperature affects the selectivity of the electrochemical CO_2 reduction on copper. *ACS. Catal.* **2023**, *13*, 8080-91. DOI PubMed PMC

46. Xu, Z.; Shen, C.; Yan, P.; et al. Temperature-driven selectivity control in bi-catalyzed CO_2 electroreduction via local alkalinity and water structure. *Chem. Eng. Sci.* **2026**, *330*, 123874. DOI